



Radiative cooling of a spin ensemble

B. Albanese¹, S. Probst¹, V. Ranjan¹, C. W. Zollitsch², M. Pechal³, A. Wallraff³, J. J. L. Morton²,
D. Vion¹, D. Esteve¹, E. Flurin¹ and P. Bertet¹✉

Physical systems reach thermal equilibrium through energy exchange with their environment, and for spins in solids the relevant environment is almost always their host lattice. However, recent studies¹ motivated by observations by Purcell² have shown how radiative emission into a microwave cavity can become the dominant relaxation path for spins if the spin-cavity coupling is sufficiently large (such as for small-mode-volume cavities). In this regime, the cavity electromagnetic field overrides the lattice as the dominant environment, inviting the prospect of controlling the spin temperature independently from that of the lattice, by engineering a suitable cavity field. Here, we report on precisely such control over spin temperature, illustrating a novel and universal method to increase the electron spin polarization above its thermal equilibrium value (termed hyperpolarization). By switching the cavity input between resistive loads at different temperatures we can control the electron spin polarization, cooling it below the lattice temperature. Our demonstration uses donor spins in silicon coupled to a superconducting microresonator and we observe more than a twofold increase in spin polarization. This approach provides a general route to signal enhancement in electron spin resonance, or nuclear magnetic resonance through dynamical nuclear spin polarization^{3,4}.

When a physical system is coupled to several reservoirs at different temperatures, it equilibrates at an intermediate temperature that depends on the strength with which it is coupled to each bath. An electron spin in a solid is coupled to two different reservoirs: phonons in its host lattice and microwave photons in its electromagnetic environment. The strength of this coupling is characterized by the rate at which the spin, of Larmor frequency ω_{spin} , relaxes by spontaneously emitting a quantum of energy $\hbar\omega_{\text{spin}}$ into each bath. In usual magnetic resonance experiments⁵, the spin-lattice relaxation rate Γ_{phon} (caused either by inelastic scattering of high-energy phonons or direct phonon emission and absorption^{6,7}) is many orders of magnitude larger than the radiative relaxation rate Γ_{phot} , so the spin temperature T_{spin} is determined by the sample temperature T_{phon} , regardless of the temperature T_{phot} of the microwave photons.

The strength of radiative relaxation can, however, be enhanced by coupling the spins resonantly to one mode of a microwave resonator of frequency $\omega_0 = \omega_{\text{spin}}$, as discovered by Purcell^{2,8,9}. The coupling strength is then given by $\Gamma_{\text{phot}} = 4g^2/\kappa$, where g is the spin-photon coupling constant and κ is the resonator mode relaxation rate. Superconducting microresonators can be designed with a small mode volume, which increases g , while retaining a high quality factor, which reduces κ . This makes it possible to reach the Purcell regime defined by $\Gamma_{\text{phot}} \gg \Gamma_{\text{phon}}$, as demonstrated in recent experiments¹. In this regime, T_{spin} should thus be equal to T_{phot} and no longer to T_{phon} , and electron spin hyperpolarization should be possible by cooling the microwave field down to a temperature $T_{\text{phot}} \ll T_{\text{phon}}$.

The simplest way to do so is to connect the resonator input to a cold $50\ \Omega$ resistor, as shown in Fig. 1a. As long as the coupling rate of the resonator field κ_{ext} to this cold reservoir at temperature T_{cold} is larger than the coupling rate $\kappa_{\text{int}} = \kappa - \kappa_{\text{ext}}$ to the hot reservoir consisting of its internal losses at temperature T_{int} , the resonator field temperature is lowered, which in turn cools the spins (Fig. 1a).

To infer T_{spin} , we use the fact that the amplitude of a spin echo is proportional to the population difference $(N_{\uparrow} - N_{\downarrow}) \equiv \Delta N$, where N_{\uparrow} and N_{\downarrow} are the number of spins in the ground and excited states, respectively. For an ensemble of $N = N_{\uparrow} + N_{\downarrow}$ spin-1/2, $\Delta N = Np(T_{\text{spin}})$, where $p(T_{\text{spin}}) = \tanh(\hbar\omega_{\text{spin}}/2kT_{\text{spin}})$ the temperature-dependent spin polarization¹⁰.

Another key measurable quantity is the rate Γ_1 at which the spins return to thermal equilibrium. In the Purcell regime, this rate $\Gamma_1 = [2\bar{n}(T_{\text{phot}}) + 1]\Gamma_{\text{phot}}$ is expected to be temperature-dependent because the rate of absorption and stimulated emission of microwave photons by each spin depends on the average intra-resonator thermal photon number $\bar{n}(T_{\text{phot}}) = 1/[e^{\hbar\omega_0/kT_{\text{phot}}} - 1]$ (refs. 8,11,12). Noting that $1/[2\bar{n}(T_{\text{phot}}) + 1] = \tanh(\hbar\omega_{\text{spin}}/2kT_{\text{phot}})$, we thus expect $\Gamma_1(T_{\text{phot}})/\Gamma_1(0) = p(0)/p(T_{\text{phot}}) = [2\bar{n}(T_{\text{phot}}) + 1]$ in the Purcell regime, an interesting prediction that we test in this work.

This radiative spin cooling scheme requires that across the temperature range between T_{cold} and T_{phon} , spins are in the Purcell regime ($\Gamma_{\text{phot}} \gg \Gamma_{\text{phon}}$) and the resonator is over-coupled ($\kappa_{\text{ext}} \gg \kappa_{\text{int}}$). Here, we use the electron spin of donors in Si, which have a low spin-lattice relaxation rate $\Gamma_{\text{phon}} \approx 10^{-4}$ – $10^{-3}\ \text{s}^{-1}$ below 1 K at 5–10 GHz (refs. 13,14), coupled to a superconducting microresonator in Nb, whose internal losses κ_{int} are very low in the same temperature interval, to demonstrate radiative spin cooling from $T_{\text{phon}} \approx 0.85\ \text{K}$ using a cold load at $T_{\text{cold}} = 20\ \text{mK}$.

The device geometry is depicted in Fig. 1b. The Nb resonator consists of an inter-digitated capacitor shunted by a 2- μm -wide inductive wire. It is patterned on top of a Si substrate in which Bi atoms have been implanted over a $\sim 1\ \mu\text{m}$ depth. The sample is mounted in a Cu holder and coupled capacitively to a microwave antenna that sets the coupling rate κ_{ext} such that $\kappa_{\text{ext}} \approx 10\kappa_{\text{int}}$ (see Methods). A d.c. magnetic field B_0 is applied parallel to the sample surface, along the inductor (z axis), to tune the spin resonance by the Zeeman effect. The resonator inductance generates a spatially inhomogeneous microwave magnetic field B_1 , which results in a spatial dependence of the spin-resonator coupling constant g shown in Fig. 1b (see Methods). This leads to a variation of the spin rotation angles and also relaxation rates Γ_{phot} throughout the sample, which are taken into account in the simulations discussed below.

The donor spin Hamiltonian $H = -\gamma_e B_0 S_z + \gamma_n B_0 I_z + AS \cdot I$ describes the Zeeman shift of the $S=1/2$ ($I = 9/2$) electron (nuclear) spin of the bismuth donor with a gyromagnetic ratio $\gamma_e/2\pi = 28\ \text{GHz T}^{-1}$ ($\gamma_n/2\pi = 6.9\ \text{MHz T}^{-1}$) and their hyperfine interaction of strength $A/2\pi = 1.45\ \text{GHz}$ (refs. 15,16). In the low-field

¹Quantronics Group, SPEC, CEA, CNRS, Université Paris-Saclay, Gif-sur-Yvette, France. ²London Centre for Nanotechnology, University College London, London, UK. ³Department of Physics, ETH Zurich, Zurich, Switzerland. ✉e-mail: patrice.bertet@cea.fr

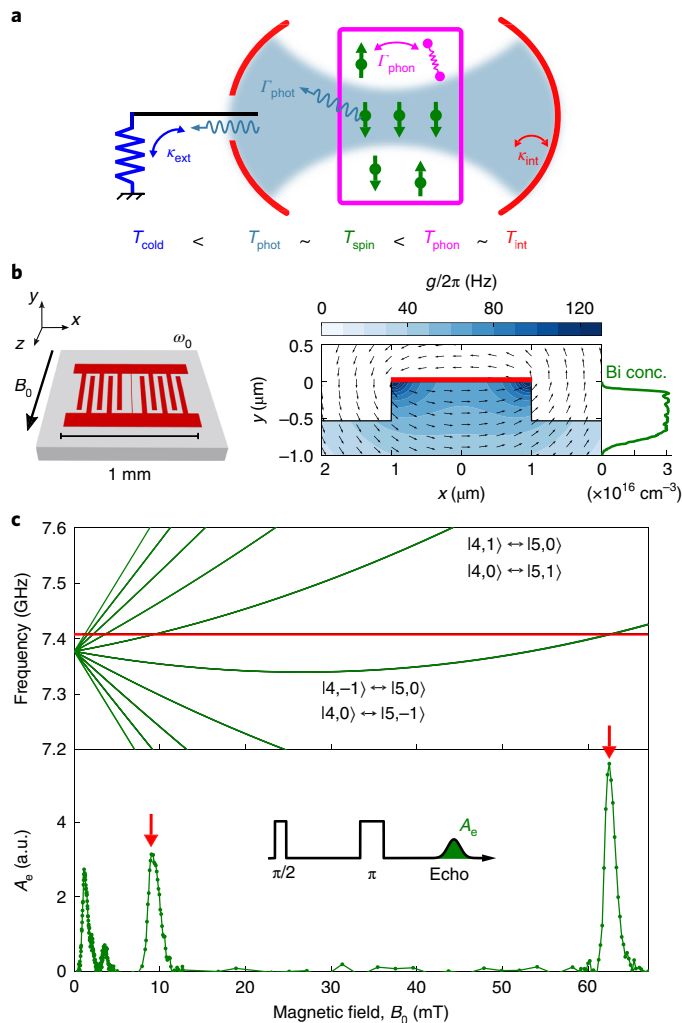


Fig. 1 | Radiative spin cooling principle and energy spectrum of Bi donors in Si.

a, Principle of the experiment. Spins (green) in a crystal (magenta) are coupled both to a bath of phonons at temperature T_{phon} with rate Γ_{phon} and to a bath of microwave photons at temperature T_{phot} with rate Γ_{phot} that determine their equilibrium temperature T_{spin} . The temperature T_{phot} is in turn determined by their coupling with rate κ_{int} to the cavity internal losses at temperature T_{int} , and with rate κ_{ext} to the load located at the cavity input. When this load is placed at a low temperature T_{cold} the intra-cavity field is radiatively cooled provided $\kappa_{\text{ext}} \gg \kappa_{\text{int}}$, and the spins are cooled in turn if $\Gamma_{\text{phot}} \gg \Gamma_{\text{phon}}$. **b**, Left: a 50-nm-thick Nb superconducting resonator (red) of frequency ω_0 is fabricated on a Si chip where Bi atoms are implanted. A static magnetic field B_0 is applied parallel to the central inductor wire of the resonator. Right: device cross-section around the inductor wire (red) and the donor implantation profile (green curve). Note that part of the substrate (~500 nm) was etched during resonator fabrication, as shown. The spin-photon coupling constant g (colour code) is represented in the Bi-doped region together with the normalized B_z field vector (arrows) generated by the inductor current. **c**, Top: solid green lines are calculated electron spin resonance transitions of the Bi donors. The resonator frequency, $\omega_0/2\pi = 7.408$ GHz (red line), is resonant with six transitions in the 0–70 mT range. Bottom: measured spin echo amplitude A_e as a function of B_0 (green line and symbols), showing the expected transitions.

regime, $\gamma_e B_0 \lesssim A$, the 20 energy eigenstates are hybridized electro-nuclear spin states, characterized by the eigenvalues F of the total angular momentum $\mathbf{F} = \mathbf{I} + \mathbf{S}$ and m of its projection along z , F_z . They can be grouped into an $F=4$ ground-state manifold of nine

states and an $F=5$ excited-state manifold of 11 states, separated by ~ 7.38 GHz (see Methods). All $\Delta m = \pm 1$ transitions are allowed in this regime; the dependence of their frequency on B_0 is shown in Fig. 1c. Corresponding peaks are observed in an echo-detected field sweep (Fig. 1c), with linewidths ranging from 0.4 to 1.3 mT (see Methods). Data in the following are obtained either at $B_0 = 62.5$ mT on the quasi-degenerate $|F=4, m=-1\rangle \leftrightarrow |5, 0\rangle$ and $|4, 0\rangle \leftrightarrow |5, -1\rangle$ transitions or at $B_0 = 9.5$ mT on the seemingly quasi-degenerate $|4, 1\rangle \leftrightarrow |5, 0\rangle$ and $|4, 0\rangle \leftrightarrow |5, 1\rangle$ transitions; each of them is treated in the following as the transition of an effective spin-1/2 system (see Methods).

In a first experiment, we measured the spin polarization p and relaxation time Γ_1^{-1} as a function of temperature T , in a set-up ensuring that $T_{\text{phot}} = T_{\text{phon}} = T_{\text{spin}} = T_{\text{int}} = T$ (Fig. 2a). As shown in Fig. 2b, we first apply a π pulse to excite the spins, let them relax during a varying time Δt , and finally measure a Hahn echo whose integral A_e is proportional to $\Delta N(\Delta t) = Np(T_{\text{spin}})(1 - 2e^{-\Gamma_1^{-1}\Delta t})$, a pulse sequence known as inversion recovery⁵. Echo curves are shown in Fig. 2b for $\Delta t \ll \Gamma_1^{-1}$ and $\Delta t \gg \Gamma_1^{-1}$, measured at $T = 20$ mK. The phase of the short- Δt echo is inverted with respect to the long- Δt echo, as expected. The shape of the short- Δt echo is due to the dependence of the Rabi angle on detuning and is well reproduced by simulations (Fig. 2b). Figure 2b shows $A_e(\Delta t)$ at 20 mK. The curve is well fitted by an exponential decay of time constant $\Gamma_1^{-1} = 5.9$ s (dashed curve), in excellent agreement with a complete simulation of the experiment that considers Purcell relaxation without any adjustable parameter (solid blue curve), confirming that the donors are in the Purcell regime at 20 mK. We measured $A_e(\Delta t)$ for varying temperatures T ; an exponential fit then yields both the relaxation time $\Gamma_1^{-1}(T)$ as well as the steady-state spin echo area $A_e(T)$. Both quantities are shown in Fig. 2c, with a scale evidencing their similar temperature dependence, in quantitative agreement with the expected $1/[2\bar{n}(T) + 1]$ dependence. This demonstrates that the Bi donor spins are in the Purcell regime at least up to 1 K.

The set-up for radiative spin cooling is presented in Fig. 3a. The device is now thermally anchored at the still stage of the dilution refrigerator, so that $T_{\text{phon}} = 0.85$ K. We use an electromechanical switch to connect the resonator input, via a superconducting coaxial cable, to a 50 Ω resistor thermalized either also at the still stage (hot configuration), that is at T_{phon} , or at the mixing chamber of the cryostat (cold configuration, $T_{\text{cold}} = 20$ mK). The field leaking from or reflected onto the cavity is routed via a circulator (also anchored at the still temperature) towards the detection chain, where it is first amplified by a Josephson travelling-wave parametric amplifier¹⁷. Microwave control pulses are sent into the cavity via a 20 dB directional coupler. This ensures that the temperature of the microwave radiation field incident onto the resonator, and therefore T_{phot} , is dominantly determined by the switch setting.

We first estimate the temperature $T_{\text{phot}}^{\text{cold}}$ of the intra-cavity field when the switch is connected to the cold load, using a series of noise measurements described in the Methods, similar to recent work^{18,19}. We obtain $T_{\text{phot}}^{\text{cold}} = 500 \pm 60$ mK, proving that the microwave field is indeed cooled radiatively, but that this cooling is only partial, which we attribute to the presence of microwave losses α between the cold load and the resonator at temperature T_{phon} (see Methods and Extended Data Fig. 1).

Hahn echoes are then measured for the two different switch settings, under otherwise identical conditions (drive pulse amplitude and repetition time). As shown in Fig. 3b, the echo amplitude more than doubles when the resonator is connected to the cold load, which demonstrates radiative spin hyperpolarization with $\eta \equiv p^{\text{cold}}/p^{\text{hot}} = 2.3 \pm 0.1$. We also measure Γ_1^{-1} in the two switch configurations, and find that $\Gamma_1^{\text{hot}}/\Gamma_1^{\text{cold}} = \eta$, as expected. Contrary to the energy relaxation time, the coherence time T_2 is not affected by the switch settings, as demonstrated in Fig. 3c, which shows $A_e(2\tau)$ for both configurations. The decay is Gaussian in both cases, with

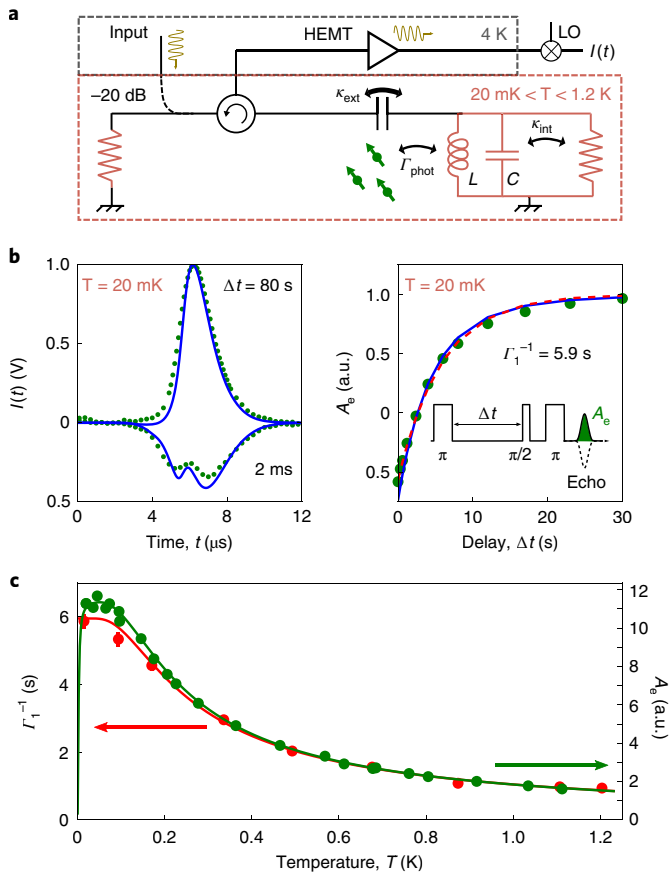


Fig. 2 | Temperature dependence of spin relaxation rate and polarization. **a**, Set-up schematic. The spins, the LC resonator to which they are coupled and the cold load are all thermalized to the same temperature T , measured with a calibrated sensor. Microwave pulses are sent to the cavity input via a -20 dB coupler. The reflected signal, with the spin echo, is amplified at 4 K by a high-electron-mobility-transistor amplifier (HEMT) and demodulated at room temperature, yielding the time-dependent quadrature $I(t)$. **b**, Measured (green dots) and simulated (blue line) echo signals (left) at short and long Δt , as well as integrated echo A_e (right) as a function of Δt , both at $T = 20 \text{ mK}$ and $B_0 = 62.5 \text{ mT}$. More details on the simulations are provided in the Methods (Extended Data Fig. 3). The pulse sequence is shown in the right panel. The red dashed curve is an exponential fit with $\Gamma_1^{-1} = 5.9 \text{ s}$. **c**, Measured relaxation time Γ_1^{-1} (red dots) and integrated echo A_e (green dots) as a function of temperature T , at $B_0 = 62.5 \text{ mT}$. The detailed measurement procedure is explained in the Methods. The red curve is a fit to the $\Gamma_1^{-1}(T)$ data between 0.3 K and 1 K using the function $\Gamma_f^{-1}/[2\bar{n}(T) + 1]$, with Γ_f^{-1} as adjustable parameter. The green curve is a fit to the $A_e(T)$ data between 0.3 K and 1 K using the function $A_f \Delta N(T)$, where $\Delta N(T)$ is the expected population difference for the transition considered and A_f is the adjusted parameter. The green curve deviates from the red below 0.2 K due to the 20 levels of the Bi donor system.

a characteristic time $T_2 = 600 \mu\text{s}$, due to spectral diffusion in the bath of ^{29}Si nuclear spins^{15,20}. This confirms that the change in echo amplitude in Fig. 3b is due to enhanced spin polarization, rather than to a change in T_2 .

The measured cooling efficiency $\eta = 2.3$ corresponds to a spin temperature $T_{\text{spin}}^{\text{cold}} = 350 \pm 10 \text{ mK}$, which is close to (or even slightly lower than) the field temperature $T_{\text{phot}}^{\text{cold}}$ estimated from noise measurements. This proves that spin–lattice relaxation is not the factor limiting spin cooling, and that the spins thermalize to the temperature of their electromagnetic environment within the accuracy of

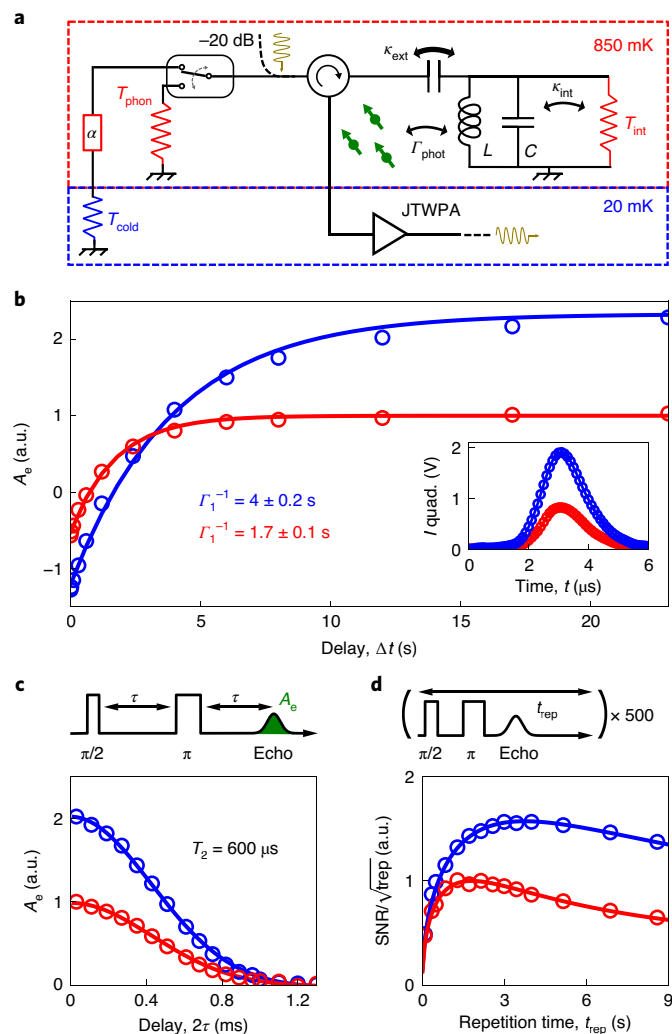
the experiment. The spin temperature achieved is explained by $\alpha = 0.23 \pm 0.03$, corresponding to $1.15 \pm 0.15 \text{ dB}$ loss at 850 mK , a plausible value for the combined effect of circulator insertion losses, the directional coupler contribution and possible spurious reflections due to impedance mismatch in the line.

The sensitivity enhancement obtained by radiative spin hyperpolarization does not scale like η as in other hyperpolarization schemes such as dynamical nuclear spin polarization (DNP), but only as $\sqrt{\eta}$, because the optimal waiting time t_{rep} between subsequent experimental sequences, which is of the order Γ_1^{-1} , also scales as η , as seen above. We demonstrate this by measuring the mean value and standard deviation of A_e for 500 echo traces as a function of the repetition time t_{rep} (Fig. 3d). The highest sensitivity is obtained for $t_{\text{rep}} \approx 1.25[\Gamma_1^{\text{cold,hot}}]^{-1}$, both in the cold and the hot load cases. It is 1.6 times larger in the cold than in the hot configuration, slightly larger than $\sqrt{\eta} = 1.52$ because switching to the cold load also substantially reduces the effective noise temperature of our detection chain (by 7%).

To test how this radiative hyperpolarization functions in the presence of other relaxation mechanisms, we introduce a relaxation rate Γ_{IR} by applying infrared illumination to the sample (using a 950 nm light-emitting diode (LED)), known to reduce the spin relaxation time of donors¹³. First, we see that the overall spin relaxation time Γ_1^{-1} , measured in the hot configuration, is indeed observed to decrease with the LED bias current I (Fig. 4a), and from this we can determine $\Gamma_{\text{IR}}^{-1}(I)$. We then measure the cooling efficiency $\eta(I)$ (Fig. 4a). At large LED powers, radiative spin cooling stops working, as expected ($\eta \approx 1$), because spins relax dominantly by interaction with the charge carriers in the substrate, whose presence is unaffected by the switch settings. The $\eta(I)$ dependence predicted by our model agrees semi-quantitatively with the data. The ratio of relaxation times $\Gamma_1^{\text{hot}}(I)/\Gamma_1^{\text{cold}}(I)$ also closely follows the measured $\eta(I)$, as expected.

We finally investigate the spin polarization dynamics (Fig. 4b). For that we replace the electromechanical switch with a superconducting device mounted at 20 mK , able to switch in a few nanoseconds without heating²¹. At 9.5 mT , the area A_e of a Hahn echo is measured at delay Δt after the switch configuration is changed, either from cold to hot or vice versa. The relaxation times in the two cases are expected to be the two values of $\Gamma_{\text{phot}}(2\bar{n}(T^{\text{cold,hot}}) + 1)$ determined by the new thermal photon population after the switching. An exponential fit of the two curves gives $(\Gamma_1^{\text{hot}})^{-1} = 3.7 \text{ s}$ and $(\Gamma_1^{\text{cold}})^{-1} = 6.4 \text{ s}$. The approximate equality of the two measured ratios, $\Gamma_1^{\text{hot}}/\Gamma_1^{\text{cold}} = 1.7$ and $p^{\text{cold}}/p^{\text{hot}} = 1.5$, is again in agreement with our model. The reduced η with respect to the previously presented result is explained by a measured 3 dB insertion loss of the superconducting switch.

We now come to the limitations and potential real-world applications of our scheme. Cooling the spins while keeping the sample hot is useful in situations where large cooling powers are needed, for example in spin-based microwave–optical transduction experiments, which require large optical powers²². One limitation of the present scheme is that the lowest spin temperature that could possibly be reached (in a lossless set-up) is the temperature T_{cold} at which the cold load is thermally anchored. However, one could also imagine cooling the resonator field using parametric processes in a circuit quantum electrodynamics platform, as recently demonstrated in ref. ²³. This would enable cooling of the resonator field and thus the spins to arbitrarily low temperatures, an appealing perspective for magnetic resonance. Such an active radiative cooling scheme could work even in ^4He cryostats with a base temperature of $1.5\text{--}4 \text{ K}$, as in standard low-temperature electron paramagnetic resonance (EPR) spectrometers. Even higher operating temperatures could be envisioned by using high- T_c superconducting thin films, although the microwave losses caused by quasiparticles may be an issue²⁴.



Regarding applications to magnetic resonance spectroscopy, we first note that, to our knowledge, the only other existing electron spin hyperpolarization method is optical illumination, which requires spin systems with very specific level schemes^{25–28}, in

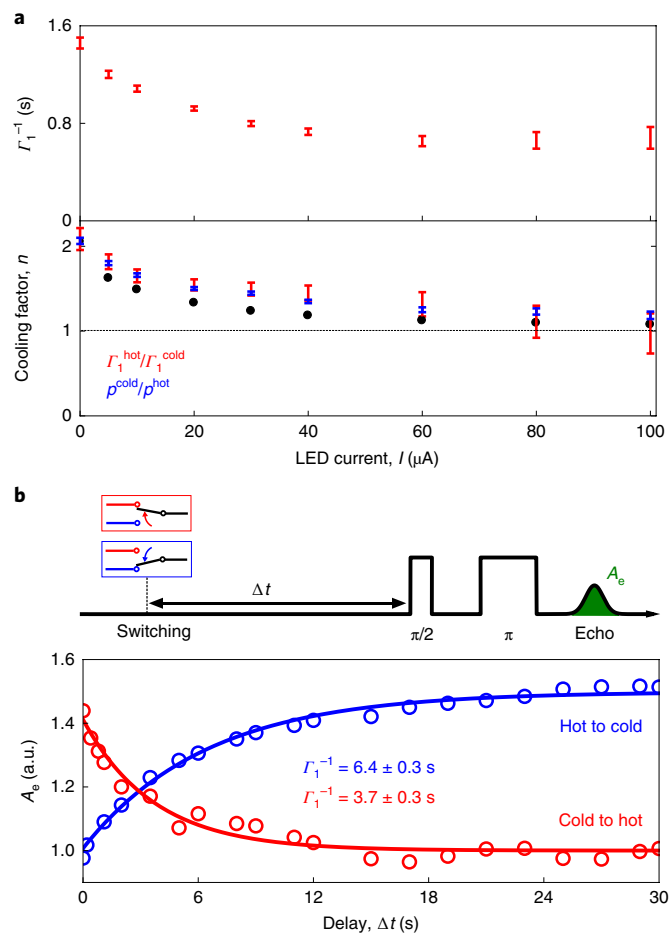


Fig. 4 | Suppression of cooling by carrier injection, and cooling dynamics.

a, Top: spin relaxation time Γ_1^{-1} , measured with an inversion recovery sequence in the hot configuration, as a function of the current I through the LED. Bottom: measured cooling factor η (blue) and $\Gamma_1^{\text{hot}} / \Gamma_1^{\text{cold}}$ (red) as a function of I . The black dots are the prediction of the model described in the main text. Error bars are estimated from the standard deviation of the exponential fit parameters. **b**, Measured integrated echo area A_e (open circles) at 9.5 mT as a function of the waiting time Δt between a rapid change of switch configuration and the echo sequence shown at the top. Solid lines are exponential fits, yielding $\Gamma_1^{-1} = 6.4 \pm 0.3$ s from hot to cold (blue) and $\Gamma_1^{-1} = 3.7 \pm 0.3$ s from cold to hot (red).

contrast to our method, which only makes use of the spin transition. A broad set of EPR measurements (including field sweeps, g -tensor measurements, HYSCORE, DEER, ENDOR and so on) could benefit from an increase in sensitivity of at least $\sqrt{\eta}$, translating into a measurement time shorter by a factor of η , obtained by radiative hyperpolarization. Only those EPR studies where the spin–lattice relaxation rate is itself the object of interest would be excluded from this approach. Regarding suitable spin species, the key requirement is for the spins to be in the Purcell regime. At cryogenic temperatures, electron spin–lattice relaxation times $\Gamma_{\text{phon}}^{-1}$ are typically in the 10^{-3} – 10^3 s range^{29–31}, so that a Purcell time $\Gamma_{\text{phot}}^{-1} \approx 10^{-2}$ s, which has already been demonstrated with a different resonator geometry³², would be sufficient for many species. The method could also be fruitfully applied to the radicals used in DNP as polarizing agents, and might enable us to obtain large nuclear spin enhancement factors in less demanding conditions than those usually required⁴ (lower magnetic field, lower microwave frequency or higher temperature).

Online content

Any methods, additional references, Nature Research reporting summaries, source data, extended data, supplementary information, acknowledgements, peer review information; details of author contributions and competing interests; and statements of data and code availability are available at <https://doi.org/10.1038/s41567-020-0872-2>.

Received: 29 October 2019; Accepted: 10 March 2020;

Published online: 20 April 2020

References

1. Bienfait, A. et al. Controlling spin relaxation with a cavity. *Nature* **531**, 74–77 (2016).
2. Purcell, E. M. Spontaneous emission probabilities at radio frequencies. *Phys. Rev.* **69**, 681 (1946).
3. Abragam, A. & Goldman, M. Principles of dynamic nuclear polarisation. *Rep. Prog. Phys.* **41**, 395–467 (1978).
4. Ardenkjær-Larsen, J. H. et al. Increase in signal-to-noise ratio of 10,000 times in liquid-state NMR. *Proc. Natl Acad. Sci. USA* **100**, 10158–10163 (2003).
5. Schweiger, A. & Jeschke, G. *Principles of Pulse Electron Paramagnetic Resonance* (Oxford Univ. Press, 2001).
6. Budoyo, R. P. et al. Phonon-bottlenecked spin relaxation of $\text{Er}^{2+}:\text{Y}_2\text{SiO}_5$ at sub-kelvin temperatures. *Appl. Phys. Express* **11**, 043002 (2018).
7. Astner, T. et al. Solid-state electron spin lifetime limited by phononic vacuum modes. *Nat. Mater.* **17**, 313–317 (2018).
8. Butler, M. C. & Weitekamp, D. P. Polarization of nuclear spins by a cold nanoscale resonator. *Phys. Rev. A* **84**, 063407 (2011).
9. Wood, C. J., Borneman, T. W. & Cory, D. G. Cavity cooling of an ensemble spin system. *Phys. Rev. Lett.* **112**, 050501 (2014).
10. Abragam, A. *The Principles of Nuclear Magnetism* (Clarendon Press, 1961).
11. Einstein, A. Strahlungs-emission und Absorption nach der Quantentheorie. *Verhandlungen der Deutschen Physikalischen Gesellschaft* **18**, 318 (1916).
12. Haroche, S. & Raimond, J.-M. *Exploring the Quantum* (Oxford Univ. Press, 2006).
13. Feher, G. & Gere, E. A. Electron spin resonance experiments on donors in silicon. II. Electron spin relaxation effects. *Phys. Rev.* **114**, 1245–1256 (1959).
14. Tyryshkin, A. M. et al. Electron spin coherence exceeding seconds in high-purity silicon. *Nat. Mater.* **11**, 143–147 (2012).
15. Feher, G. Electron spin resonance experiments on donors in silicon. I. Electronic structure of donors by the electron nuclear double resonance technique. *Phys. Rev.* **114**, 1219–1244 (1959).
16. Mohammady, M. H., Morley, G. W. & Monteiro, T. S. Bismuth qubits in silicon: the role of EPR cancellation resonances. *Phys. Rev. Lett.* **105**, 067602 (2010).
17. Macklin, C. et al. A near-quantum-limited Josephson traveling-wave parametric amplifier. *Science* **350**, 307–310 (2015).
18. Wang, Z. et al. Quantum microwave radiometry with a superconducting qubit. Preprint at <https://arxiv.org/pdf/1909.12295.pdf> (2019).
19. Xu, M. et al. Radiative cooling of a superconducting resonator. *Phys. Rev. Lett.* **124**, 033602 (2020).
20. George, R. E. et al. Electron spin coherence and electron nuclear double resonance of Bi donors in natural Si. *Phys. Rev. Lett.* **105**, 067601 (2010).
21. Pechal, M. F. et al. Superconducting switch for fast on-chip routing of quantum microwave fields. *Phys. Rev. Appl.* **6**, 024009 (2016).
22. Williamson, L. A., Chen, Y.-H. & Longdell, J. J. Magneto-optic modulator with unit quantum efficiency. *Phys. Rev. Lett.* **113**, 203601 (2014).
23. Gely, M. F. et al. Observation and stabilization of photonic Fock states in a hot radio-frequency resonator. *Science* **363**, 1072–1075 (2019).
24. Rauch, W. et al. Microwave properties of $\text{YBa}_2\text{Cu}_3\text{O}_{7-x}$ thin films studied with coplanar transmission line resonators. *J. Appl. Phys.* **73**, 1866–1872 (1993).
25. Adrian, F. J. Theory of anomalous electron spin resonance spectra of free radicals in solution. Role of diffusion-controlled separation and reencounter of radical pairs. *J. Chem. Phys.* **54**, 3918–3923 (1971).
26. Wong, S. K., Hutchinson, D. A. & Wan, J. K. S. Chemically induced dynamic electron polarization. II. A general theory for radicals produced by photochemical reactions of excited triplet carbonyl compounds. *J. Chem. Phys.* **58**, 985–989 (1973).
27. Steger, M. et al. Quantum information storage for over 180 s using donor spins in a ^{28}Si ‘semiconductor vacuum’. *Science* **336**, 1280–1283 (2012).
28. Doherty, M. W. et al. The nitrogen-vacancy colour centre in diamond. *Phys. Rep.* **528**, 1–45 (2013).
29. Castle, J. G. & Feldman, D. W. Resonance modes at defects in crystalline quartz. *Phys. Rev.* **137**, A671–A673 (1965).
30. Gayda, J.-P. et al. Temperature dependence of the electronic spin-lattice relaxation time in a 2-iron-2-sulfur protein. *Biochim. Biophys. Acta* **581**, 15–26 (1979).
31. Zhou, Y., Bowler, B. E., Eaton, G. R. & Eaton, S. S. Electron spin lattice relaxation rates for $S=12$ molecular species in glassy matrices or magnetically dilute solids at temperatures between 10 and 300 K. *J. Magn. Reson.* **139**, 165–174 (1999).
32. Probst, S. et al. Inductive-detection electron-spin resonance spectroscopy with 65 spins/Hz^{1/2} sensitivity. *Appl. Phys. Lett.* **111**, 202604 (2017).

Publisher's note Springer Nature remains neutral with regard to jurisdictional claims in published maps and institutional affiliations.

© The Author(s), under exclusive licence to Springer Nature Limited 2020

Methods

Sample processing. The substrate is a Si sample with a natural isotopic abundance of 4.7% of ^{29}Si nuclear spins. This was implanted with Bi atoms in an energy range of 500–3,000 keV, resulting in the estimated implantation profile shown in Fig. 1b. The sample was then annealed at a temperature of 900 °C for 5 min, under nitrogen flow. Based on ref. ³⁵, we expect an activation yield of 60%. The total number of dopants was confirmed by standard EPR spectroscopy as well as conductance measurements. To fabricate the resonator, a 50-nm-thick Nb film was sputtered and subsequently etched by reactive ion etching. During the Nb etching step, part of the Si substrate was also etched (measured depth of 500 nm), which is visible in Fig. 1b.

Resonator parameters. The resonator frequency and external and internal losses were extracted from the reflection coefficient measurements performed with a vector network analyser. The data presented in this Letter were collected in different runs of the experiment. Slight variations of the resonator parameters were observed from run to run. The frequency ω_0 was seen to decrease over time due to Nb oxidation. The internal loss rate κ_{int} was observed to vary slightly from run to run, as commonly seen for dielectric losses. Variations in the external loss rate κ_{ext} from run to run were also observed, indicating a change in capacitive coupling between the resonator and the antenna that we attribute to slight changes in the thermal contractions. These changes in κ_{ext} were observed to affect the precise value of the Purcell relaxation times consistently with $\Gamma_{\text{photon}} = 4g^2/\kappa$; however, the cooling factor was found to be quite reproducible over several runs.

We now provide the values measured for each of the runs shown. Internal losses were always measured with signal power corresponding to an intra-cavity photon population close to 1. The resonator frequency values reported were obtained at $B_0 = 0$ mT. For the measurements reported in Figs. 1 and 2 and Extended Data Figs. 2 and 3, $\omega_0/2\pi = 7.40785$ GHz, $\kappa_{\text{ext}} = 3.4 \times 10^6 \text{ s}^{-1}$ and $\kappa_{\text{int}} = 2.8 \times 10^5 \text{ s}^{-1}$. For the measurements reported in Figs. 3 and 4a, the resonator parameters are $\omega_0/2\pi = 7.40815$ GHz, $\kappa_{\text{ext}} = 4.8 \times 10^6 \text{ s}^{-1}$ and $\kappa_{\text{int}} = 3.2 \times 10^5 \text{ s}^{-1}$. The data for Fig. 4b were obtained with the resonator with $\omega_0/2\pi = 7.41172$ GHz, $\kappa_{\text{ext}} = 3.2 \times 10^6 \text{ s}^{-1}$ and $\kappa_{\text{int}} = 3.2 \times 10^5 \text{ s}^{-1}$. The noise measurements of Extended Data Fig. 1 were performed with resonator parameters of $\omega_0/2\pi = 7.41014$ GHz, $\kappa_{\text{ext}} = 3.8 \times 10^6 \text{ s}^{-1}$ and $\kappa_{\text{int}} = 3.2 \times 10^5 \text{ s}^{-1}$.

Spin linewidth and cooperativity. The inhomogeneous linewidth of the Bi donor EPR transitions is visible on the echo-detected field sweep shown in Fig. 1c. We observe linewidths ranging from 0.4 mT to 1.5 mT, which we attribute to a combination of two effects. The first is the 0.4 mT Overhauser field caused by the ^{29}Si nuclear spin bath³⁰. The second source of broadening is the strain exerted by the differential thermal contraction of the superconducting thin film and the Si substrate, which was shown to affect A^{34} and therefore to broaden the Bi donor linewidth³⁵. The ensemble cooperativity was measured to be ~ 0.005 – 0.01 by determining the additional cavity losses when a Bi donor transition was tuned in resonance at ω_0 . The cooperativity being lower than one implies that spins can be considered as radiating independently from each other¹.

Thermalization of a system coupled to N bosonic baths. When a physical system exchanges energy with an environment consisting of N reservoirs at different temperatures T_j , the intermediate effective temperature T_{sys} at which the system equilibrates depends on the strength Γ_j with which it is coupled to each bath, defined as the rate at which the system would spontaneously relax from its first excited state to its ground state by emitting a quantum of energy into this bath at zero temperature. For a system coupled to N bosonic reservoirs, T_{sys} is obtained by

$$\bar{n}(T_{\text{sys}}) = \sum_{j=1}^N (\Gamma_j/\Gamma) \bar{n}(T_j) \quad (1)$$

where $\bar{n}(T) = 1/[\exp(\hbar\omega_0/kT) - 1]$ is the occupation number of a bosonic mode at frequency ω_0 , and $\Gamma = \sum_{j=1}^N \Gamma_j$ the total system–bath coupling. If the system is dominantly coupled to one bath j_0 ($\Gamma_{j_0} \gg \Gamma_{j \neq j_0}$), the system therefore equilibrates close to T_{j_0} regardless of the temperature of the other reservoirs.

Cavity thermal photon population. The resonator mode of frequency ω_0 is coupled by internal dissipation of rate κ_{int} to a hot thermal bath at T_{int} , not necessarily equal to the sample temperature T_{photon} , and by the external losses of rate κ_{ext} to the thermal radiation in the propagating input mode, whose temperature T_{ext} is determined by the switch state. From equation (1) we get $\bar{n}(T_{\text{photon}}) = (\kappa_{\text{int}}/\kappa) \bar{n}(T_{\text{int}}) + (\kappa_{\text{ext}}/\kappa) \bar{n}(T_{\text{ext}})$, where $\kappa = \kappa_{\text{int}} + \kappa_{\text{ext}}$. In the same way, when the switch is in the cold configuration, the input mode is coupled to the cold bath at T_{cold} and, as a consequence of losses and impedance mismatches modelled by the absorption factor α , to the hot bath at T_{photon} . The thermal occupation of the input mode at ω_0 in the cold state is then an average of the hot and cold bath populations expressed as $\bar{n}(T_{\text{cold}}) = (1 - \alpha) \bar{n}(T_{\text{cold}}) + \alpha \bar{n}(T_{\text{photon}})$. In the present experiment $T_{\text{cold}} = 20$ mK, therefore $\bar{n}(T_{\text{cold}}) \approx 0$. Substituting $\bar{n}(T_{\text{cold}})$ in the expression of $\bar{n}(T_{\text{photon}})$, the average number of resonator thermal photons in the cold case is found to be $\bar{n}(T_{\text{photon}}^{\text{cold}}) \approx \frac{\kappa_{\text{int}}}{\kappa} \bar{n}(T_{\text{int}}) + \frac{\alpha \kappa_{\text{ext}}}{\kappa} \bar{n}(T_{\text{photon}})$. When in the hot case, $\bar{n}(T_{\text{ext}}^{\text{hot}}) = \bar{n}(T_{\text{photon}})$ and $\bar{n}(T_{\text{photon}}^{\text{hot}}) = (\kappa_{\text{int}}/\kappa) \bar{n}(T_{\text{int}}) + (\kappa_{\text{ext}}/\kappa) \bar{n}(T_{\text{photon}})$.

Spin effective temperature T_{spin} and cooling factor η . The spins are coupled with strength Γ_{photon} to the resonator mode populated by thermal photons, and with strength Γ_{photon} to the lattice phonon mode of occupation number $\bar{n}(T_{\text{photon}})$. From equation (1), the spin temperature is defined as $\bar{n}(T_{\text{spin}}) = (\Gamma_{\text{photon}}/(\Gamma_{\text{photon}} + \Gamma_{\text{photon}})) \bar{n}(T_{\text{photon}}) + (\Gamma_{\text{photon}}/(\Gamma_{\text{photon}} + \Gamma_{\text{photon}})) \bar{n}(T_{\text{photon}})$. As discussed in the main text for the Purcell rate, a spin coupled to a bosonic mode of temperature T_j with strength Γ_j relaxes at a rate $\Gamma_1 = \Gamma_j(2\bar{n}(T_j) + 1)$ as a consequence of absorption and emission rate dependence on the thermal population of the mode. The relaxation rate of the spins coupled to the effective bath of temperature T_{spin} is then $\Gamma_1 = (\Gamma_{\text{photon}} + \Gamma_{\text{photon}})(2\bar{n}(T_{\text{spin}}) + 1) = \Gamma_{\text{photon}}(2\bar{n}(T_{\text{photon}}) + 1) + \Gamma_{\text{photon}}(2\bar{n}(T_{\text{photon}}) + 1)$, that is, the sum of the spin–photon and spin–lattice relaxation rates, as expected. On the other hand, the polarization of the spins at temperature T_{spin} is $p(T_{\text{spin}}) = 1/(2\bar{n}(T_{\text{spin}}) + 1) = (\Gamma_{\text{photon}}(2\bar{n}(T_{\text{photon}}) + 1)/\Gamma_1) p(T_{\text{photon}}) + (\Gamma_{\text{photon}}(2\bar{n}(T_{\text{photon}}) + 1)/\Gamma_1) p(T_{\text{photon}})$, so equal to the equilibrium polarizations at the two baths' temperatures weighted by the corresponding relaxation rates. The cooling factor, defined as the ratio of the equilibrium polarization in the two switch states, is therefore still equal to the ratio of total relaxation rates as for purely Purcell relaxation, $\eta = \frac{\Gamma_{\text{photon}}(2\bar{n}(T_{\text{photon}}) + 1) + \Gamma_{\text{photon}}(2\bar{n}(T_{\text{photon}}^{\text{hot}}) + 1)}{\Gamma_{\text{photon}}(2\bar{n}(T_{\text{photon}}) + 1) + \Gamma_{\text{photon}}(2\bar{n}(T_{\text{photon}}^{\text{cold}}) + 1)}$. In this work we assume Γ_{photon} to be negligible, in agreement with the result of simulations.

Under illumination by the infrared LED, a new relaxation process of rate $\Gamma_{\text{IR}}(I)$ is introduced. Neglecting Γ_{photon} , the cooling factor model $\eta(I)$ used to fit the data in Fig. 4b is then $\eta(I) = \frac{\Gamma_{\text{IR}}(I) + \Gamma_{\text{photon}}(2\bar{n}(T_{\text{photon}}^{\text{hot}}) + 1)}{\Gamma_{\text{IR}}(I) + \Gamma_{\text{photon}}(2\bar{n}(T_{\text{photon}}^{\text{cold}}) + 1)}$.

Measurement of cavity mode temperature. Measuring the noise power spectral density S in the output mode yields an estimate of the resonator mode temperature. $S(\omega, T_{\text{photon}})$ was measured in a 6 MHz bandwidth around ω_0 for T_{photon} ranging from 840 mK to 1.16 K in both switch configurations. A lower resonator quality factor in the cold than in the hot configuration, measured at $B_0 = 0$, points to a reduced temperature of the internal losses $T_{\text{int}}^{\text{cold}} < T_{\text{int}}^{\text{hot}}$ possibly due to cooling of the electric dipoles coupled to the resonator. We therefore consider the general case of resonator internal losses temperature, $T_{\text{int}} \neq T_{\text{photon}}$. In the hot configuration then, $S^{\text{hot}}/G(\omega)\hbar\omega = (1 - \beta(\omega)) \bar{n}(T_{\text{photon}}) + \beta(\omega) \bar{n}(T_{\text{int}}^{\text{hot}}) + 1/2 + n_{\text{TWPA}}$, where $G(\omega)$ is the known frequency-dependent total gain of the output line, n_{TWPA} is the noise added by the TWPA and $\beta(\omega) = 4\kappa_{\text{int}}\kappa_{\text{ext}}/(\kappa^2 + 4(\omega - \omega_0)^2)$ is the transmission function. On the other hand, the expression of S in the cold case is $S^{\text{cold}}/G(\omega)\hbar\omega = \alpha(1 - \beta(\omega)) \bar{n}(T_{\text{photon}}) + \beta(\omega) \bar{n}(T_{\text{int}}^{\text{cold}}) + 1/2 + n_{\text{TWPA}}$. A first fit of $S^{\text{hot}}(T_{\text{photon}})$ gives $n_{\text{TWPA}} = 0.75 \pm 0.25$. By then fitting $S^{\text{hot}}(\omega)$ for each value of T_{photon} we obtain the corresponding $T_{\text{int}}^{\text{hot}}$, while α and $T_{\text{int}}^{\text{cold}}$ result from the fit of $S^{\text{cold}}(\omega)$. The temperature T_{int} of the resonator internal losses is found to be $\sim 10\%$ larger (lower) than T_{photon} values in the hot (cold) configuration. For all T_{photon} values we extract $\alpha \approx 0.47 \pm 0.1$ (note that this value differs from the one given in the main text because of the slight difference between the estimated spin temperature and the cavity field temperature estimated from the noise measurements). The extracted parameters allow us to calculate the cavity thermal photon population using $\bar{n}(T_{\text{photon}}^{\text{hot}}) = (\kappa_{\text{ext}}/\kappa) \bar{n}(T_{\text{photon}}) + (\kappa_{\text{int}}/\kappa) \bar{n}(T_{\text{int}}^{\text{hot}})$ and $\bar{n}(T_{\text{photon}}^{\text{cold}}) = \alpha(\kappa_{\text{ext}}/\kappa) \bar{n}(T_{\text{photon}}) + (\kappa_{\text{int}}/\kappa) \bar{n}(T_{\text{int}}^{\text{cold}})$ in the hot and cold configuration, respectively. The effective intra-cavity field temperature of $T_{\text{photon}}^{\text{hot}} = 850$ mK and $T_{\text{photon}}^{\text{cold}} = 500 \pm 60$ mK are then found at $T_{\text{photon}} = 840$ mK, corresponding to a predicted cooling factor of $\eta = 1.65 \pm 0.2$ for the spins. The measurement of S therefore confirms that the spin cooling efficiency is limited by the temperature of the intra-cavity mode rather than non-radiative spin relaxation phenomena.

Bi donors in Si. The spin Hamiltonian of Bi donors in Si includes a Zeeman effect and an isotropic hyperfine coupling: $H/h = \mathbf{B} \cdot (-\gamma \mathbf{S} \otimes \mathbf{1} + \gamma_n \mathbf{1} \otimes \mathbf{I}) + AS \cdot \mathbf{I}$, where $\gamma/2\pi = 27.997$ GHz is the electronic gyromagnetic ratio, $\gamma_n/2\pi = 6.9$ MHz is the nuclear gyromagnetic ratio and $A/h = 1.475$ GHz is the hyperfine coupling constant. For low applied static magnetic field aligned along z ($B_0 \hat{y} \ll A$), the eigenstates of \mathbf{S} and \mathbf{I} are highly hybridized and the energy eigenbasis is $|F, m\rangle$, in which $\mathbf{F} = \mathbf{S} + \mathbf{I}$ is the total angular momentum of eigenvalue F and F_z its projection along \mathbf{B}_0 with eigenvalue m . An oscillating field along x or y can therefore excite transitions satisfying $\Delta F \Delta m = \pm 1$, whose matrix elements $\langle F, m | S_x | F + 1, m \pm 1 \rangle = \langle F, m | S_y | F + 1, m \pm 1 \rangle$ are comparable in magnitude with the ideal electronic spin 1/2 transition $\langle -1/2 | S_x | 1/2 \rangle = 0.5$. We note here that in the $-4 < m \leq 4$ manifold the $|F, m - 1\rangle \leftrightarrow |F + 1, m\rangle$ and $|F, m\rangle \leftrightarrow |F + 1, m - 1\rangle$ transitions are quasi-degenerate in frequency and the sum of their associated S_x matrix elements is equal to 0.5. The spectrum consists then of six resolvable transitions for $B_0 < 100$ mT, as shown in Fig. 1c. At zero field the nine ground ($F = 4$) and 11 excited ($F = 5$) multiplets are separated by a frequency of 7.38 GHz. For B_0 going from 0 to 65 mT, the hyperfine splitting within the two multiplets $E_{\text{hyperf}} = E_{|F, m+1\rangle} - E_{|F, m\rangle}$ increases from 0 to ~ 150 MHz.

Population difference $\Delta N(T)$ for Bi donors. The magnetic resonance signal is proportional to the population unbalance $\Delta N = N_+ - N_-$, where N_+ (N_-) is the total number of spins in the excited (ground) state of the spin transition considered. In the case of Bi donors, where the electron spin transitions $|4, m\rangle \leftrightarrow |5, m - 1\rangle$ and $|4, m - 1\rangle \leftrightarrow |5, m\rangle$ (for $-4 < m \leq 4$) are quasi-degenerate in frequency compared

to the resonator linewidth, $\Delta N(T_{\text{spin}})$ is the population unbalance between the two excited and two ground states: $\Delta N(T_{\text{spin}}) = N(p_{|4,m\rangle} + p_{|4,m-1\rangle} - p_{|5,m\rangle} - p_{|5,m-1\rangle})$, where N is the total number of donors and $p_{|F,m\rangle} = e^{-E_{F,m}/kT_{\text{spin}}}/Z$ is the occupation probability of $|F, m\rangle$, with $Z = \sum_{F,m} e^{-E_{F,m}/kT_{\text{spin}}}$ the partition function. The green line in Fig. 2 shows $\Delta N(T)$ for the transition considered.

As long as $T_{\text{spin}} > 100$ mK and $B_0 < 70$ mT, the thermal energy is much larger than the energy difference between hyperfine states of both $F=5$ and $F=4$ manifolds $E_{|F,m\rangle} - E_{|F,m-1\rangle}$. In that case, one can show that

$$\Delta N(T_{\text{spin}}) \simeq \frac{N}{9} \frac{1 + e^{-\hbar\omega_0/kT_{\text{spin}}}}{1 + 11/9e^{-\hbar\omega_0/kT_{\text{spin}}}} \tanh(\hbar\omega_0/2kT_{\text{spin}}),$$

by $\frac{N}{10} \tanh(\hbar\omega_0/2kT_{\text{spin}})$, especially when $kT_{\text{spin}} > \hbar\omega_0$, which happens in our case for $T_{\text{spin}} > 300$ mK. This is visible in Fig. 2c, where the computed $\Delta N(T)$ (green curve) indeed coincides well with the result for a spin-1/2 $\tanh(\hbar\omega_0/2kT_{\text{spin}})$ (red curve) for $T_{\text{spin}} > 300$ mK (by proper choice of the scale for A_c).

Temperature dependence of polarization for transitions $|4, -1\rangle \leftrightarrow |5, 0\rangle$ and $|4, 0\rangle \leftrightarrow |5, -1\rangle$. We first measure the temperature dependence of polarization at $B_0 = 62.5$ mT, waiting several hours at each temperature value before measuring the echo amplitude A_c . The result reported in Extended Data Fig. 2 (red circles) shows a significant deviation below 200 mK from the calculated $\Delta N(T)$ (red line). Spins are then in a non-thermal state below 200 mK, possibly due to residual infrared radiation reaching the sample. This is known to cause redistribution of population in the Bi hyperfine levels³⁶. We repeat then the same measurement by adding, at each temperature point, a first step during which we set $B_0 = 9.3$ mT for 20 min before setting the field back to 62.5 mT. Four minutes after the field is set to 62.5 mT, we measure A_c . The result is reported in both Fig. 1c (green dots) and Extended Data Fig. 2 (black circles) and is in good agreement with the calculated $\Delta N(T)$ for the same transitions and $B_0 = 9.3$ mT. This shows that at lower field the spins reach thermal equilibrium while the depolarizing phenomenon taking place at 62.5 mT is not effective. In a third measurement performed at $T = 83$ mK, we first set $B_0 = 9.3$ mT for 20 min, then we set $B_0 = 62.5$ mT and immediately after this we record A_c continuously as a function of time. The result reported in the inset of Extended Data Fig. 2 shows the spins reaching the equilibrium non-thermal state in a timescale of hours, orders of magnitude longer than the 4 min waiting time used to detect the thermal equilibrium polarization after a field sweep from 9.3 mT to 62.5 mT.

Estimate of single spin coupling g . The interaction of the individual Bi donor spins with the resonator mode of frequency ω_0 is described by the Jaynes–Cummings Hamiltonian $H = \hbar g(\sigma^+ a + \sigma^- a^\dagger)$, where σ^+ (σ^-) is the spin raising (lowering) operator, a (a^\dagger) is the annihilation (creation) operator for intra-cavity photons, and g is the spin–photon coupling strength. All the spin echo measurements in the present work, unless specified, are performed at 62.5 mT on the $|4, -1\rangle \leftrightarrow |5, 0\rangle$ and $|4, 0\rangle \leftrightarrow |5, -1\rangle$ quasi-degenerate transitions, whose matrix elements are equal to 0.28 and 0.22, respectively. As a consequence, two families of spins are probed simultaneously, with different coupling strengths given by $g = \gamma_e \langle F, m | S_y | F + 1, m - 1 \rangle |\delta B_1|$, where δB_1 is the magnitude of the magnetic field vacuum fluctuations at the spin location generated by the current vacuum fluctuations δ_i in the resonator inductor wire. The value of δ_i is given by $\delta_i = \omega_0 \sqrt{\hbar/2Z_0}$, where $Z_0 = \sqrt{L/C} = 46 \Omega$ is the characteristic impedance of the LC resonator estimated from electromagnetic simulation realized in CST Microwave Studio. To obtain δB_1 in the Si substrate around the inductor, we perform simulation of the magnetic field generated by δ_i using COMSOL software. A non-uniform distribution of the current density in the superconducting Nb wire is assumed. The so-obtained spatial distribution of the coupling constant $g(x, y)$ for the $|4, 0\rangle \leftrightarrow |5, -1\rangle$ transition is shown in Fig. 1b. Combining $g(x, y)$ for the two transitions with the spin implantation profile (Fig. 1b), we extract the coupling distribution density of the spin ensemble $\rho(g)$ (Extended Data Fig. 3a) that we use in the spin simulation to reproduce the Hahn echo measurements.

Spin simulation. The simulation of the dynamics of the spin ensemble weakly coupled to the intra-cavity field consists in numerical solution of the system semi-classical equation of motion, as described in ref. 37. The system of differential equations is solved for M values of coupling g and the results are averaged using $\rho(g)$ as a weighting function. The transverse relaxation time is fixed to the measured T_2 , while the longitudinal relaxation rate is imposed for each g value to be the Purcell rate, $\Gamma_1 = \frac{\gamma_e^2 \hbar^2}{\delta^2 \tau} \frac{1}{4 + \delta^2 \tau^2}$, where $\delta = \omega_{\text{spin}} - \omega_0$ is the spin–cavity detuning. The spin distribution in frequency is modelled as a square centred at ω_0 and 3 MHz wide. Simulation of Rabi oscillations driven by varying the amplitude of the second pulse in the Hahn echo sequence is shown in Extended Data Fig. 3b. The average of signals emitted by spins with different Rabi frequencies results in damped oscillations that are in qualitative agreement with the experimental data. The pulse amplitude giving the maximum signal is then chosen as the π -pulse amplitude for simulation of the inversion recovery sequence.

Pulse sequences. All the A_c data points presented in this work, excepted the SNR measurement, are obtained using a Hahn echo sequence followed by a

Carr–Purcell–Meiboom–Gill sequence (CPMG). From 100 to 300 π pulses are therefore applied after the first echo to record as many additional echoes, which are then averaged to improve the SNR. The π -pulse length is fixed to 250 ns, double with respect to the $\pi/2$ pulse. The amplitude of the two pulses is always the same while the phase of the π pulses is 90° shifted. The spectrum presented in Fig. 1d is measured with a delay $\tau = 8 \mu\text{s}$ between the $\pi/2$ pulse and the π pulse, with 10 additional CPMG π pulses separated by 16 μs and a repetition time t_{rep} of 5.8 s. The measurement is averaged 32 times at each B_0 field value. The Γ_1 measurements of Fig. 2 are realized with $\tau = 15 \mu\text{s}$, 300 CPMG pulses separated by 2τ and $t_{\text{rep}} = 80$ s. At each temperature, the Γ_1^{-1} measurement is repeated eight times and then averaged. The echo amplitude as a function of temperature, shown in Fig. 2c, is obtained with $\tau = 15 \mu\text{s}$, $t_{\text{rep}} = 120$ s, 300 CPMG pulses separated by 2τ and no further averaging. For the Γ_1 measurement of Fig. 3, $\tau = 15 \mu\text{s}$, $t_{\text{rep}} = 120$ s, 100 CPMG pulses are separated by 2τ and no further averaging is used. In the T_2 experiment of Fig. 3c, $t_{\text{rep}} = 10$ s, 300 CPMG pulses separated by 8 μs are used and each data point is averaged four times. The pulse sequence of each echo sample in the SNR experiment of Fig. 3d does not include CPMG and has $\tau = 15 \mu\text{s}$. Figure 4a shows the results of Γ_1 measurements realized with $\tau = 15 \mu\text{s}$, $t_{\text{rep}} = 40$ s and 300 CPMG pulses separated by 2τ . At each LED I , the Γ_1 measurement is repeated four times and then averaged. The cooling and recovery dynamics of Fig. 4b are instead measured using $\tau = 19.5 \mu\text{s}$, $t_{\text{rep}} = 30$ s, 100 CPMG pulses separated by 2τ and 20 averages of each data point.

Data availability

Source data are available for this paper. All other data that support the plots within this paper and other findings of this study are available from the corresponding author upon reasonable request.

References

- Weis, C. D. et al. Electrical activation and electron spin resonance measurements of implanted bismuth in isotopically enriched silicon-28. *Appl. Phys. Lett.* **100**, 172104 (2012).
- Mansir, J. et al. Linear hyperfine tuning of donor spins in silicon using hydrostatic strain. *Phys. Rev. Lett.* **120**, 167701 (2018).
- Pla, J. et al. Strain-induced spin-resonance shifts in silicon devices. *Phys. Rev. Appl.* **9**, 044014 (2018).
- Sekiguchi, T. et al. Hyperfine structure and nuclear hyperpolarization observed in the bound exciton luminescence of Bi donors in natural Si. *Phys. Rev. Lett.* **104**, 137402 (2010).
- Ranjan, V. et al. Pulsed electron spin resonance spectroscopy in the purcell regime. *J. Magn. Reson.* **310**, 106662 (2020).

Acknowledgements

We thank P. Sénat, D. Duet and J.-C. Tack for technical support, and are grateful for discussions within the Quantronics group. We acknowledge IARPA and Lincoln Labs for providing a Josephson travelling-wave parametric amplifier. We acknowledge support from the European Research Council through grant no. 615767 (CIRQUSS) and through the Superconducting Quantum Networks project, the Agence Nationale de la Recherche under the Chaire Industrielle NASNIQ, the Region Ile-de-France via DIM SIRTEQ, the Engineering and Physical Sciences Research Council (EPSRC) through grant no. EP/K025945/1, the Horizon 2020 research and innovation programme through grant no. 771493 (LOQO-MOTIONS), the National Centre of Competence in Research ‘Quantum Science and Technology’, a research instrument of the Swiss National Science Foundation, and the ETH Zurich.

Author contributions

B.A., S.P. and P.B. designed the experiment. J.J.L.M. and C.W.Z. provided and characterized the implanted Si sample, on which B.A. and S.P. fabricated the Nb resonator. B.A. performed the measurements, with help from S.P. and V.R. B.A. and P.B. analysed the data. B.A. and V.R. performed the simulations. M.P. realized and tested the superconducting switch in a project guided by A.W. B.A. and P.B. wrote the manuscript. S.P., V.R., A.W., J.J.L.M., D.V., D.E. and E.F. contributed useful input to the manuscript.

Competing interests

The authors declare no competing interests.

Additional information

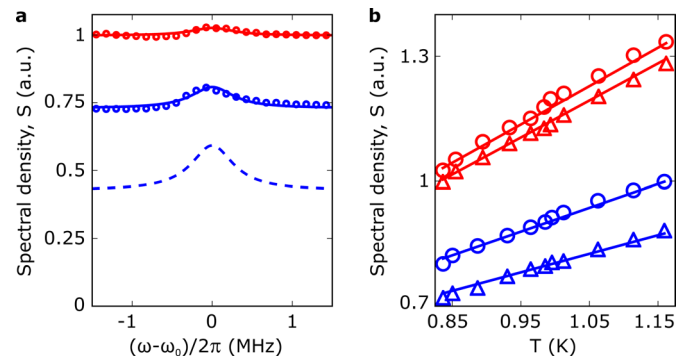
Extended data is available for this paper at <https://doi.org/10.1038/s41567-020-0872-2>.

Supplementary information is available for this paper at <https://doi.org/10.1038/s41567-020-0872-2>.

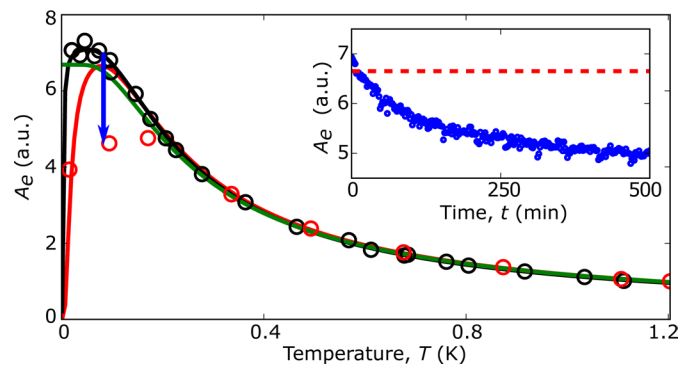
Correspondence and requests for materials should be addressed to P.B.

Peer review information *Nature Physics* thanks Stefan Putz and other, anonymous, reviewer(s) for their contribution to the peer review of this work.

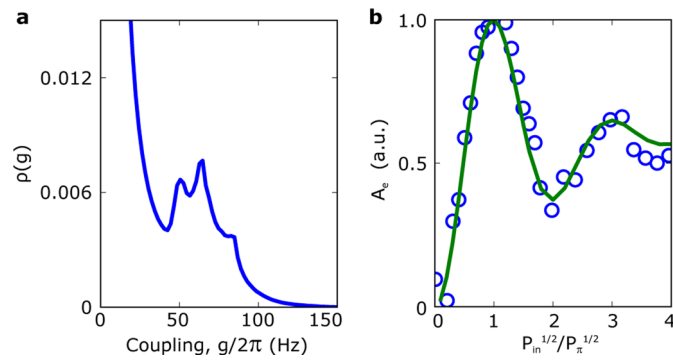
Reprints and permissions information is available at www.nature.com/reprints.



Extended Data Fig. 1 | Noise power spectral density measurement. **a**, Frequency dependence of the noise power spectral density S measured at $T_{\text{phon}}=840$ mK for the *hot* (red circles) and *cold* (blue circles) switch configurations. Solid lines are fit (see Methods). The blue dashed line indicates the expected $S^{\text{cold}}(\omega)$ for $\alpha=0$. **b**, Still temperature T_{phon} dependence of S measured at $\omega = \omega_0$ (open circles) and at $\omega - \omega_0 = -2.7$ MHz (open triangles) for both hot (red) and cold (blue) configurations. Solid lines are plot of S^{hot} (red) and S^{cold} (blue) with parameters obtained from the frequency dependence fits performed at all T_{phon} and with $n_{\text{TWPA}} = 0.75$.



Extended Data Fig. 2 | Temperature dependence of polarization. Equilibrium polarization of transitions $|4, -1\rangle \leftrightarrow |5, 0\rangle$ and $|4, 0\rangle \leftrightarrow |5, -1\rangle$ measured at $B_0=62.5$ mT (red circles). Several hours are waited at each temperature before recording A_e . Red line is the calculated $\Delta N(T)$ for the considered transition at $B_0=62.5$ mT. A second polarisation measurement of the same transitions (black circles) is reported. In this experiment, for each temperature value, B_0 is first set to 9.3 mT during 20 min, then it is set to 62.5 mT and finally after 4 min A_e is recorded. The black line is the calculated $\Delta N(T)$ for the considered transition at $B_0=9.3$ mT. The polarisation $p(T)=\tanh(\frac{h\nu_0}{2kT})$ of a spin 1/2 is also shown for comparison (green). A_e as a function of time (inset) is measured at $T=83$ mK and $B_0=62.5$ mT after B_0 has been set to 9.3 mT for 20 min. The same data are represented in the main plot with the blue arrow.



Extended Data Fig. 3 | Simulation of Rabi oscillations. **a**, Distribution of the spin-cavity coupling g obtained from the spatial distribution of δB_1 . **b**, Rabi oscillations measured at $B_0=62.5$ mT and $T=850$ mK by varying the amplitude of the second pulse in the Hahn echo sequence (blue circles). The pulse amplitude is normalized to the value $P_{\pi}^{1/2}$ corresponding to the maximum in detected signal. The solid green line is the result of the numerical simulation of a spin ensemble described by $\rho(g)$.